

# An Acceptor–Donor–Acceptor Structured Nano-Aggregate for NIR-Triggered Interventional Photoimmunotherapy of Cervical Cancer

Gaoli Niu, Xingqi Bi, Yong Kang, Hua Zhao, Ruiyan Li, Mengbin Ding, Baoli Zhou, Yanhong Zhai, Xiaoyuan Ji,\* and Yongsheng Chen

Compared with conventional therapies, photoimmunotherapy offers precise targeted cancer treatment with minimal damage to healthy tissues and reduced side effects, but its efficacy may be limited by shallow light penetration and the potential for tumor resistance. Here, an acceptor–donor–acceptor (A–D–A)-structured nanoaggregate is developed with dual phototherapy, including photodynamic therapy (PDT) and photothermal therapy (PTT), triggered by single near-infrared (NIR) light. Benefiting from strong intramolecular charge transfer (ICT), the A–D–A-structured nanoaggregates exhibit broad absorption extending to the NIR region and effectively suppressed fluorescence, which enables deep penetration and efficient photothermal conversion ( $\eta = 67.94\%$ ). A suitable HOMO–LUMO distribution facilitates sufficient intersystem crossing (ISC) to convert ground-state oxygen ( $^3\text{O}_2$ ) to singlet oxygen ( $^1\text{O}_2$ ) and superoxide anions ( $\cdot\text{O}_2^-$ ), and catalyze hydroxyl radical ( $\cdot\text{OH}$ ) generation. The enhanced ICT and ISC effects endow the A–D–A structured nanoaggregates with efficient PTT and PDT for cervical cancer, inducing efficient immunogenic cell death. In combination with clinical aluminum adjuvant gel, a novel photoimmunotherapy strategy for cervical cancer is developed and demonstrated to significantly inhibit primary and metastatic tumors in orthotopic and intraperitoneal metastasis cervical cancer animal models. The noninvasive therapy strategy offers new insights for clinical early-stage and advanced cervical cancer treatment.

rates in moderately developed countries.<sup>[1]</sup> Globally, 300 000 people die unnecessarily each year.<sup>[2]</sup> Photoimmunotherapy (PIT) has emerged as a cutting-edge approach to cancer treatment that combines the specificity of immunotherapy with the precision of light-based therapy, including photothermal therapy (PTT) and photodynamic therapy (PDT).<sup>[3]</sup> PIT utilizes photosensitizing agents conjugated to tumor-targeting antibodies or ligands, which selectively bind to cancer cells expressing specific antigens.<sup>[4]</sup> Upon illumination with near-infrared (NIR) light, these conjugates induce rapid and selective cancer cell death through the generation of cytotoxic reactive oxygen species (ROS) or other phototoxic mechanisms while sparing adjacent healthy tissues.<sup>[5]</sup> This targeted cytotoxicity not only eliminates primary tumors but also activates antitumor immune responses, leading to systemic tumor regression and potential long-term immune memory.<sup>[6]</sup> With its ability to precisely target tumor cells while activating robust immune responses, PIT represents a promising paradigm shift in cancer therapy with the potential to improve patient outcomes and overcome the limitations of traditional treatments.<sup>[7]</sup> Moreover, given the unique physiological structure of cervical cancer, fiber-optic-assisted PIT is expected to become a new generation of clinical strategies for treating cervical cancer.<sup>[8]</sup>

## 1. Introduction

According to 2022 global cancer statistics, cervical cancer ranks among the top five in terms of both incidence and mortality

traditional treatments.<sup>[7]</sup> Moreover, given the unique physiological structure of cervical cancer, fiber-optic-assisted PIT is expected to become a new generation of clinical strategies for treating cervical cancer.<sup>[8]</sup>

G. Niu, Y. Kang, R. Li, M. Ding, B. Zhou, X. Ji  
 Academy of Medical Engineering and Translational Medicine  
 Medical College  
 Tianjin University  
 Tianjin 300072, China  
 E-mail: [jixiaoyuan@tju.edu.cn](mailto:jixiaoyuan@tju.edu.cn)

G. Niu, Y. Zhai  
 The First Affiliated Hospital of Henan Polytechnic University  
 Jiaozuo 454000, China

X. Bi, Y. Chen  
 State Key Laboratory and Institute of Elemento-Organic Chemistry  
 The Centre of Nanoscale Science and Technology and Key Laboratory of  
 Functional Polymer Materials  
 Renewable Energy Conversion and Storage Center (RECAST)  
 Tianjin Key Laboratory of Functional Polymer Materials  
 College of Chemistry  
 Nankai University  
 Tianjin 300071, China

 The ORCID identification number(s) for the author(s) of this article can be found under <https://doi.org/10.1002/adma.202407199>

DOI: 10.1002/adma.202407199

The efficiency of inducing immunogenic death of tumor cells by phototherapy is the key to PIT. PDT and PTT utilize nontoxic photosensitizing agents and harmless NIR light to induce cancer cell death through the generation of ROS or hyperthermia.<sup>[9]</sup> While PDT harnesses ROS such as singlet oxygen to target cancer cells, PTT employs hyperthermia to achieve similar effects.<sup>[3b,10]</sup> Despite their individual efficacy, both modalities face limitations, such as the susceptibility of PDT to hypoxia in the tumor microenvironment and the potential of PTT for collateral damage to healthy tissues.<sup>[5a,11]</sup> The combination of PDT and PTT, known as dual phototherapy,<sup>[12]</sup> offers synergistic advantages, including enhanced tumor penetration, minimized side effects, and improved treatment efficacy.<sup>[3b,5b,13]</sup> This innovative approach holds significant promise for overcoming the challenges associated with single-modal therapies and advancing precision cancer treatment strategies.

Dual-mode PSs, which are capable of harnessing both photothermal and photodynamic effects, have garnered significant attention in the field of cancer therapy due to their potential to enhance treatment efficacy while minimizing adverse effects on healthy tissues.<sup>[5c,7a]</sup> Several classes of dual-mode PSs, including organic molecules, inorganic nanoparticles, and hybrid materials, have been developed.<sup>[7c,14]</sup> Organic molecules such as porphyrins, phthalocyanines, and cyanine dyes exhibit excellent photothermal and photodynamic properties,<sup>[15]</sup> while inorganic nanoparticles such as gold nanoparticles and carbon nanomaterials possess unique optical properties suitable for dual-mode therapy. Hybrid materials combining organic and inorganic components offer tailored functionalities and enhanced therapeutic performance.<sup>[16]</sup> Despite their promise, dual-mode PSs face several challenges in clinical translation. One major limitation is the complexity associated with their design and synthesis, which may hinder large-scale production and increase manufacturing costs.<sup>[17]</sup> Moreover, the potential toxicity of certain photosensitizer components or degradation byproducts raises concerns regarding their safety profile and biocompatibility.<sup>[18]</sup> Furthermore, the limited penetration depth of light in tissue restricts the application of dual-mode photosensitizers to superficial tumors, limiting their efficacy in treating deep-seated or metastatic cancers.<sup>[5a]</sup> Future research efforts should focus on optimizing the design of dual-mode PSs, improving their biocompatibility, and exploring novel strategies to overcome existing limitations, thereby maximizing their potential in oncology.

A-D-A molecules, characterized by their donor-acceptor-donor molecular structure, have garnered significant interest in the field of solar cells due to their unique mechanisms and advantageous properties.<sup>[19]</sup> A-D-A molecules possess a conjugated electron system that enables efficient absorption of light across a wide spectrum, including ultraviolet to near-infrared

wavelengths.<sup>[20]</sup> Upon light absorption, these molecules undergo energy transfer processes, possibly leading to the generation of reactive species and hyperthermia, which are essential for therapeutic effects.<sup>[5b,21]</sup> Based on the A-D-A molecule developed in the field of solar cells,<sup>[22]</sup> in this study, we designed and prepared a new A-D-A structured molecule named DTPC-N2F. To increase its bioavailability, nanoparticles (DNPs) were prepared through nanoprecipitation. The outer layer was coated with cell membrane (CM) to form DNPs@CM. Benefiting from strong intramolecular charge transfer (ICT), the A-D-A structured nanoaggregates exhibit broad absorption, which can extend to the NIR region, and effectively suppress fluorescence, which enables deep penetration and efficient photothermal conversion. A suitable HOMO-LUMO distribution facilitates sufficient intersystem crossing (ISC) to convert ground-state oxygen ( $^3\text{O}_2$ ) to singlet oxygen ( $^1\text{O}_2$ ) and superoxide anions ( $\text{O}_2^-$ ).<sup>[3c,23]</sup> Under 980 nm laser excitation, these nanoparticles exhibited excellent PTT and type I and type II PDT effects. In vivo treatment was conducted in conjunction with aluminum adjuvant gel (Alum), which has a strong antigen adsorption capability, leading to sustained ICD effects. In situ, cervical cancer animal models were simulated clinically, and in situ, photoimmunotherapy was performed. This treatment not only suppressed the growth of primary tumors but also inhibited the growth of intraperitoneal metastatic tumors (Figure 1). This provides a basis for the combined immunotherapy of cervical cancer using novel A-D-A small molecule-based organic photosensitizers.

## 2. Results and Discussion

### 2.1. Preparation and Characterization of DTPC-N2F, DNPs, and DNPs@CM

The A-D-A molecule DTPC-N2F is synthesized using 9,14-dihydro-4H-dithieno [2',3':2,3;3'',2'':10,11] Piceno [1,14,13,12-*bcdefgh*] carbazole (DTPC) as the electron donor and 2-(6,7-difluoro-3-oxo-2,3-dihydro-1H-cyclopenta[*b*]naphthalen-1-ylidene) malononitrile (NINC-N2F) as the electron acceptor (Figures S1–S4, Supporting Information). The calculated molar extinction coefficient ( $\epsilon = 1.68 \times 10^5 \text{ M}^{-1} \text{ cm}^{-1}$ ) indicates that DTPC-N2F exhibits strong light absorption capability (Figure S5, Supporting Information). The HOMO electron cloud of DTPC-N2F is delocalized on the central donor unit, while the LUMO is located on the electron-deficient end group unit. This delocalized electronic structure results in DTPC-N2F having a narrow bandgap. Additionally, the separated LUMO and HOMO enable effective ICT transitions,<sup>[24]</sup> providing a basis for the photothermal and photodynamic properties of DTPC-N2F.<sup>[25]</sup> Through DFT calculations, the LUMO and HOMO of DTPC-N2F were determined to be  $-3.43$  and  $-5.10$  eV, respectively, with T1 at  $-3.98$  eV and  $\Delta E_{\text{ST}}$  at  $0.55$  eV. The  $E_g$  is calculated to be  $1.67$  eV, indicating a narrow bandgap that enhances its near-infrared light absorption capability (Figure 2A). DTPC-N2F dissolves well in common organic solvents. To facilitate biological applications, we synthesized DTPC-N2F into nanoparticles, named DNPs, using the nanoprecipitation method as documented in the literature.<sup>[26]</sup> The nanoprecipitation method is a commonly used technique for preparing nanoparticles, capable of precipitating precursor substances from solution

H. Zhao  
Henan Reproductive Hospital  
Henan Provincial People's Hospital  
People's Hospital of Zhengzhou University  
Zhengzhou, Henan 450003, China  
X. Ji  
Medical College  
Linyi University  
Linyi 276000, China

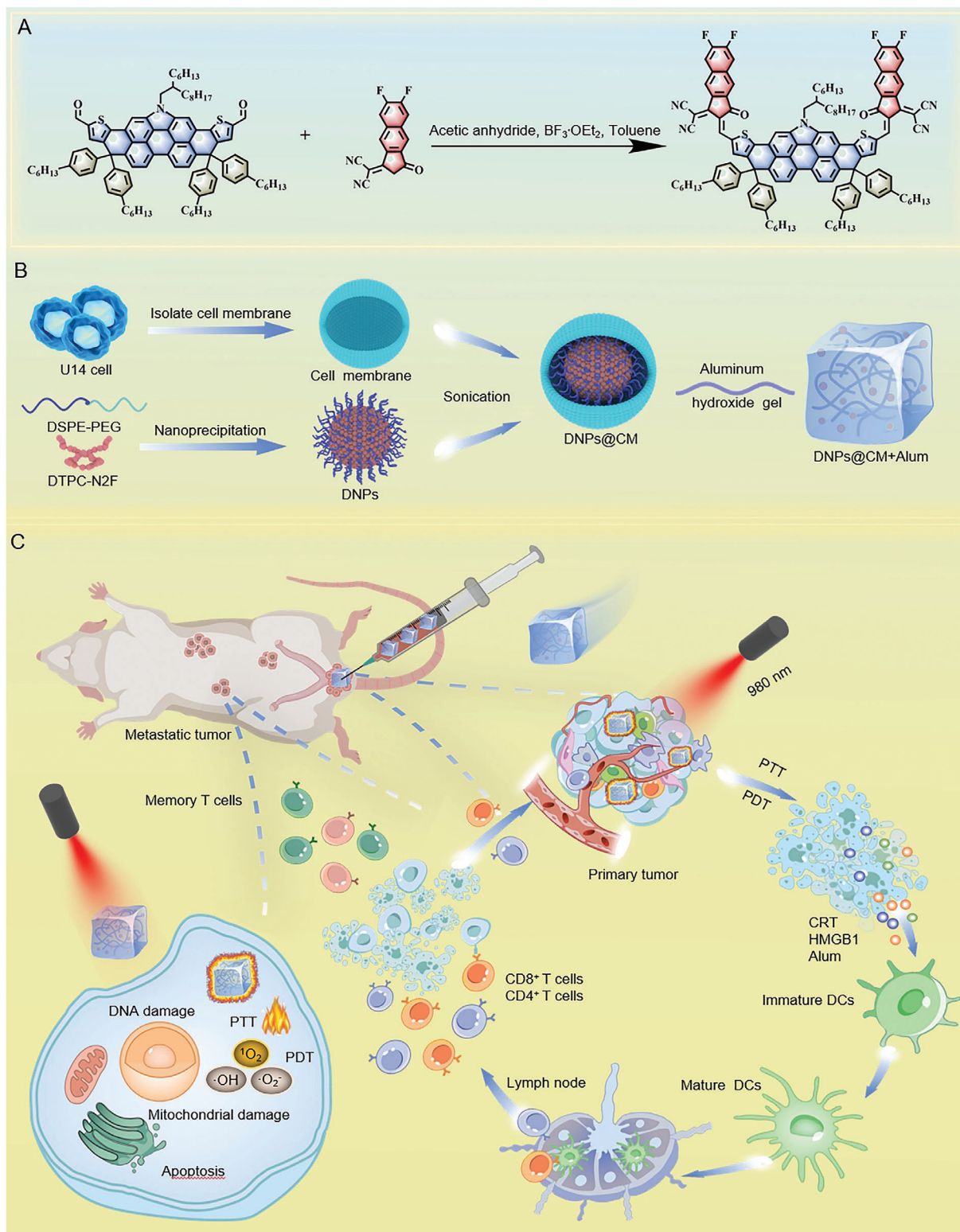


**Figure 1.** Schematic diagram of photoimmunotherapy for in situ cervical cancer treatment using DNP@CM+Alum. A) Synthesis steps of DTPC-N2F. B) Extraction of the U14 cell membrane, nanoprecipitation synthesis of DNP@CM, cell membrane encapsulation to form DNP@CM, and mixing with alum under sonication to form DNP@CM+Alum. C) 980 nm laser irradiation of DNP@CM induces apoptosis in tumor cells through photothermal and type I and type II photodynamic effects. Postirradiation, the enhanced release of tumor antigens and DAMPs combined with alum promotes sustained ICD, enhances the systemic antitumor immune response, and promotes immunological memory, thereby treating primary tumors and inhibiting the growth of peritoneal metastases.

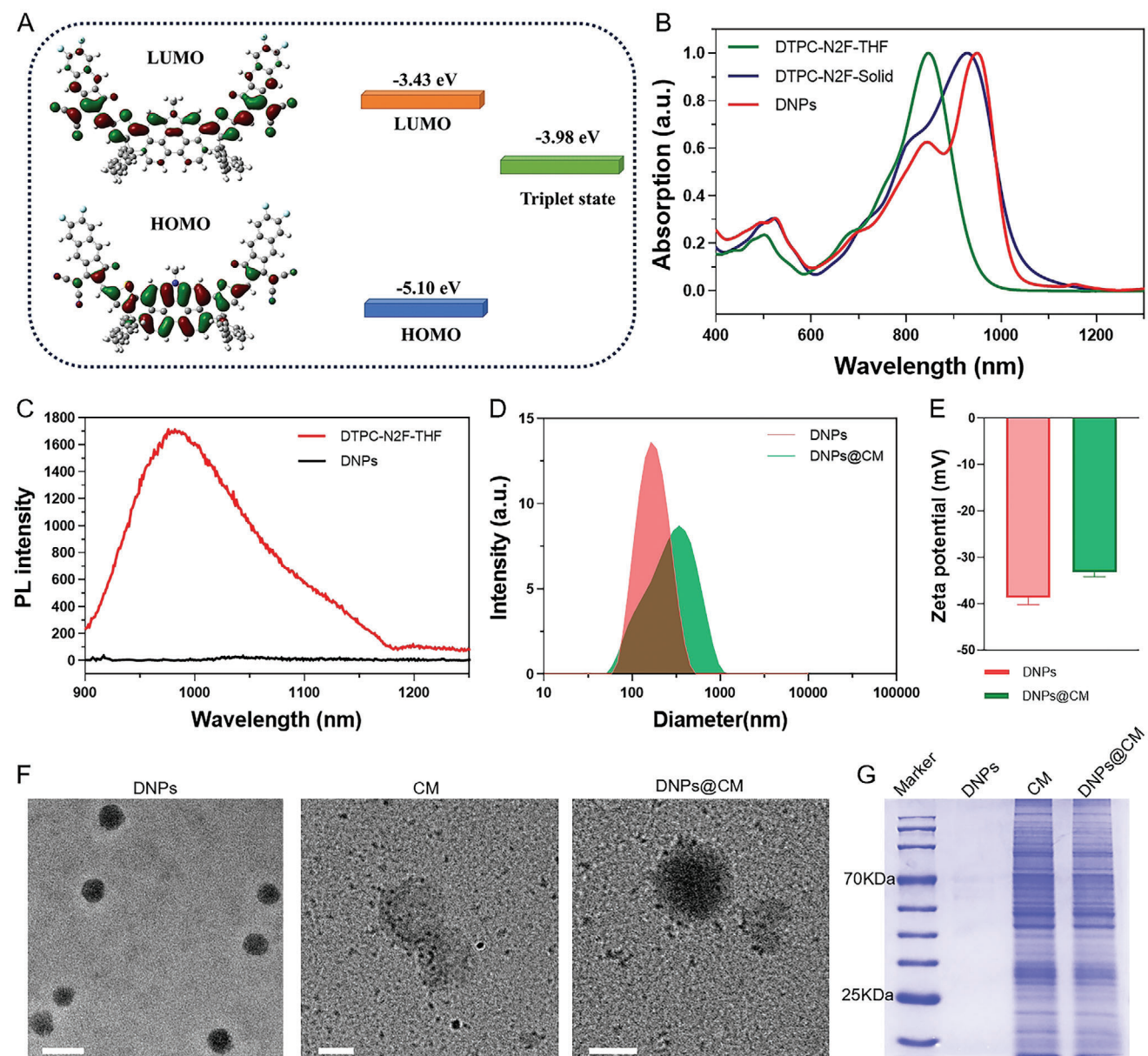


**Figure 2.** Characterization of DTPC-N2F, DNPs, and DNPs@CM. A) Calculated HOMO, LUMO, and triplet state of DTPC-N2F using the DFT B3LYP/6-31G (d) method. Energy gap ( $E_g$ ) =  $E_{LUMO} - E_{HOMO}$ . B) Normalized UV-Vis absorption spectra of DTPC-N2F dissolved in THF, solid DTPC-N2F, and DNPs. C) Fluorescence spectra of DTPC-N2F dissolved in THF ( $12.5 \mu\text{g mL}^{-1}$ ) and DNPs dispersed in water ( $12.5 \mu\text{g mL}^{-1}$ ). Hydrodynamic diameter D) and zeta potential E) data for DNPs and DNPs@CM obtained by DLS. F) TEM image of DNPs and DNPs@CM; scale bar = 200 nm. G) SDS-PAGE and Coomassie blue staining bands of DNPs, CM, and DNPs@CM.

into solid nanoparticles. The addition of DSPE-PEG5000 enhances the stability and dispersibility of the nanoparticles and improves their biocompatibility. The protective effect of PEG chains extends the circulation time of the material *in vivo*.<sup>[27]</sup> The nanoparticles (DNPs) prepared using this method exhibit good stability, with consistent particle size and surface potential across different times and batches. Additionally, the calculated photothermal conversion efficiency is also consistent, and TEM images show a highly uniform appearance (Figure S6 and Table S1, Supporting Information). To assess the changes in the photophysical properties of DTPC-N2F before and after nanoparticle

formation, UV-vis-NIR spectroscopy was employed to measure its light absorption ability. The maximum absorption peak of DTPC-N2F dissolved in Tetrahydrofuran (THF) was observed at 847 nm, while in the solid (film) form, it shifted to 928 nm. After the synthesis of DNPs, the maximum absorption peak shifted to 949 nm (Figure 2B). The reason for the red shift in the maximum absorption peak can be analyzed as follows: it is known that small molecules usually exhibit different aggregation characteristics in thin films or solid states, including H- and J-aggregation.<sup>[28]</sup> The aggregation type of these A-D-A molecules is mainly J-aggregation,<sup>[29]</sup> which leads to absorption

redshift. Compared to the solution, DTTPC-N2 exhibits strong and ordered packing in its film or nanoparticle states, which causes the absorption spectrum to redshift. A larger red shift in the absorption peak indicates that DTTPC-N2F exhibits excellent near-infrared-triggered phototherapy capability when prepared as DNPs. Fluorescence spectroscopy revealed that DTTPC-N2F dissolved in THF exhibited high fluorescence, whereas the fluorescence of the DNPs was quenched. The quenching of fluorescence implies that after DTTPC-N2F is prepared into nanoparticles (DNPs), it maximizes the conversion of light energy into heat and exhibits excellent ISC capability, thereby maximizing the effects of PTT and PDT (Figure 2C).

Lipid components and membrane proteins on the surface of tumor cell membranes can enhance the stability and antitumor immune activity of nanoparticles.<sup>[30]</sup> Therefore, mouse cervical cancer U14 cell membranes were used to coat DNPs to form DNPs@CM. Dynamic Light Scattering (DLS) tests showed that both DNPs and DNPs@CM had good dispersion properties, with the maximum hydrodynamic diameter of DNPs at 164.2 nm and that of DNPs@CM at 342 nm (Figure 2D). Zeta potential measurements revealed that both DNPs and DNPs@CM possessed significantly negative surface charges, with maximum surface charges of  $-40.4$  and  $-33.8$  mV, respectively (Figure 2E), which facilitates their colloidal stability and easier adsorption in tumors. Additionally, DNPs ( $25 \mu\text{g mL}^{-1}$ ) dissolved in Dulbecco's Modified Eagle's Medium (DMEM), water, or Phosphate-Buffered Saline (PBS) showed almost no changes in appearance or particle size after one week, indicating good stability of the DNPs (Figure S7, Supporting Information). Representative transmission electron microscopy (TEM) images revealed uniformly spherical DNPs with a particle size of  $\approx 150$  nm and extracted cell membrane particles of  $\approx 300$  nm in size, and membrane-coated nanoparticles were successfully observed (Figure 2F). The visualization of different bands after staining the extracted membrane surface proteins by sodium dodecyl sulfate-polyacrylamide gel electrophoresis (SDS-PAGE) and Coomassie blue also confirmed the successful coating of the U14 tumor cell membrane on the nanoparticles (Figure 2G).

## 2.2. Photothermal and Photodynamic effect of DNPs

This A-D-A-structured DTTPC-N2F exhibits a strong ICT effect and high molar extinction coefficient, displaying the characteristics of a narrow bandgap and strong near-infrared light capture capability. According to the simulated Jablonski diagram, DTTPC-N2F and DSPE-PEG nanoparticles coprecipitate as DNPs, leading to fluorescence quenching. Upon excitation with a 980 nm laser, PTT effects are generated through vibrational relaxation. According to calculations,  $\Delta E_{\text{ST}}$  is 0.55 eV, which promotes the conversion of ground-state oxygen ( $^3\text{O}_2$ ) into  $^1\text{O}_2$  and the generation of free radicals  $\cdot\text{O}_2^-$  and  $\cdot\text{OH}$  (Figure 3A). Under low-power, ( $0.6 \text{ W cm}^{-2}$ ) 980 nm laser irradiation, different concentrations of DNPs exhibited efficient and rapid temperature increases (Figure 3B), as recorded using an infrared thermal imager (Figure 3C). As the irradiation time and concentration increased, the temperature of the solution continued to increase. When the concentration of the DNPs solution increased to  $50 \mu\text{g mL}^{-1}$ , the temperature reached a maximum of

$55.3 \text{ }^\circ\text{C}$  after 12 min of laser exposure. At a lower concentration of  $12.5 \mu\text{g mL}^{-1}$ , under the same conditions, the temperature of the solution still increased to  $48.5 \text{ }^\circ\text{C}$ , a temperature sufficient to induce apoptosis in tumor cells. In contrast, the temperature of the PBS solution only increased from  $27.1$  to  $30.1 \text{ }^\circ\text{C}$  after 12 min of light exposure. Further tests were conducted by irradiating the same concentration of DNPs ( $50 \mu\text{g mL}^{-1}$ ) at different power levels; the temperature of the solution increased with increasing laser power density, reaching  $68.2 \text{ }^\circ\text{C}$  at  $1.0 \text{ W cm}^{-2}$  after 12 min of 980 nm laser irradiation (Figure 3D,E). The experiments demonstrated that DNPs have effective PTT effects when excited by long-wavelength light. DNPs ( $50 \mu\text{g mL}^{-1}$ ) underwent five thermal cycles in PBS, each involving 5 min of irradiation with a 980 nm laser at  $0.6 \text{ W cm}^{-2}$ . As observed in Figure 3F, the maximum temperature in each cycle exceeded  $50 \text{ }^\circ\text{C}$ , and upon turning off the laser, the temperature of the solution quickly returned to room temperature. According to the literature,<sup>[31]</sup> the photothermal conversion efficiency ( $\eta$ ) reached up to 67.94% (Figure S8, Supporting Information). To further investigate the stability of DNPs, solutions of different concentrations of DNPs ( $50, 25, 12.5 \mu\text{g mL}^{-1}$ ) were irradiated with a 980 nm laser at  $1.0 \text{ W cm}^{-2}$  for 30 min, during which the solution temperature continuously increased. The UV-Vis-NIR absorption spectra of the solutions measured before and after irradiation showed no significant change in the peak absorption at 949 nm (Figure S9, Supporting Information), confirming that the nanoparticles possess excellent photostability.

To verify the excellent type I and type II photodynamic effects of DNPs, various in vitro experiments were conducted to evaluate the ability of DNPs to generate ROS under light irradiation. First, the generation capability of  $\cdot\text{O}_2^-$  under 980 nm laser irradiation was assessed using diphenylisobenzofuran (DPBF) as a probe. Due to the efficient ISC of DNPs, the absorption peak of DPBF decreased by 80% within just 3 min as the DNPs concentration increased from 0 to  $25 \mu\text{g mL}^{-1}$ . Even at a lower concentration of  $6.25 \mu\text{g mL}^{-1}$ , the absorption peak still decreased by 60%. Significant declines in DPBF absorption were also observed under different power settings of 980 nm laser irradiation at the same DNPs concentration, showing a linear relationship with time and power (Figure 3G,H; Figure S10, Supporting Information). Next, a Singlet oxygen sensor green fluorescent probe (SOSG) was used to detect  $^1\text{O}_2$ . It was observed that the fluorescence intensity of SOSG increased with the concentration of DNPs under 980 nm laser irradiation at the same power; similarly, the fluorescence intensity of SOSG increased with the laser power at the same DNPs concentration. Both scenarios showed a linear relationship over time (Figure 3I,J; Figure S11, Supporting Information), demonstrating that DNPs exhibit outstanding photodynamic effects under 980 nm laser irradiation. In addition, 3,3',5,5'-Tetramethylbenzidine (TMB) was used to detect the production of  $\cdot\text{OH}$ . During a 10-min irradiation period, the absorption peak of TMB increased by  $\approx 80\%$  when the DNPs concentration was  $25 \mu\text{g mL}^{-1}$ . Under different power levels of 980 nm laser irradiation, the TMB absorption peak also exhibited a linear increase (Figure 3K,L; Figure S12, Supporting Information).

Using electron spin resonance (ESR) technology, the types of ROS generated were further identified. 2,2,6,6-Tetra-methylpiperidine (TEMP) was used as a spin-trapping agent. A triplet signal characteristic of TEMP-1-oxyl was

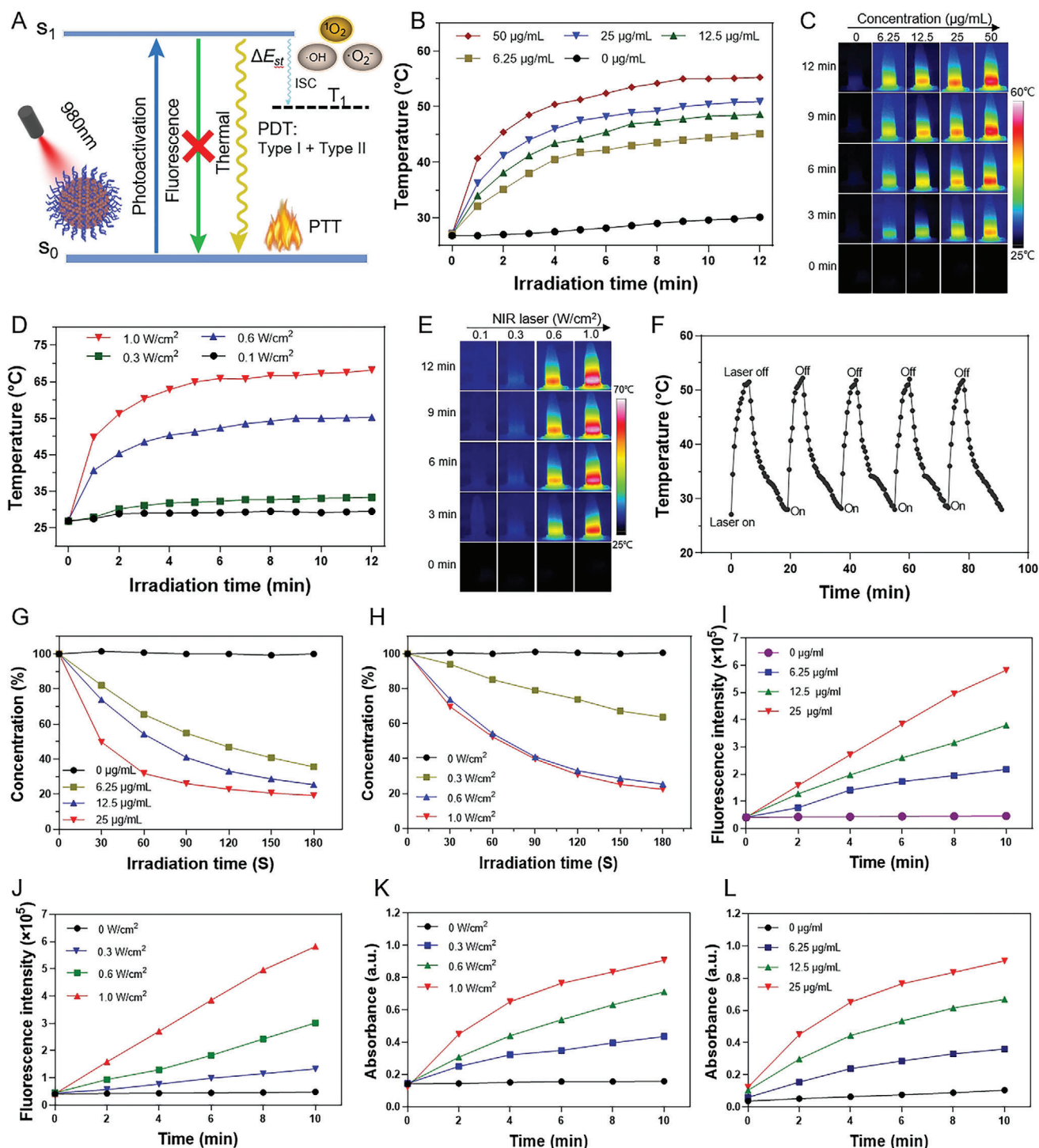


**Figure 3.** Evaluation of DNP PTT and type I and type II PDT effects. A) Modified Jablonski diagram illustrating the PTT and PDT mechanisms of DNP under 980 nm laser irradiation. Photothermal properties of DNP at different concentrations under  $0.6 \text{ W cm}^{-2}$  980 nm laser irradiation B) and infrared thermal imaging C). Temperature change curves of DNP under different power levels of 980 nm laser irradiation ( $50 \mu\text{g mL}^{-1}$ ) D) and infrared thermal imaging E). F) Temperature change curves of DNP under five cycles of 980 nm ( $0.6 \text{ W cm}^{-2}$ ) laser on-off irradiation. Evaluation of  $\cdot\text{O}_2^-$  generation after 980 nm laser irradiation of DNP was assessed by measuring DPBF intensity with different concentrations G) and different powers H). Evaluation of  $^1\text{O}_2$  generation after 980 nm laser irradiation of DNP was assessed by measuring SOSG fluorescence intensity with different concentrations I) and different powers J). Evaluation of  $\cdot\text{OH}$  generation after 980 nm laser irradiation of DNP was performed by measuring changes in TMB absorption peaks with different concentrations K) and different powers L).

detected, indicative of  $^1\text{O}_2$ . DMPO, used as a spin trap for  $\cdot\text{O}_2^-$  and  $\cdot\text{OH}$  radicals, displayed  $\cdot\text{O}_2^-$  and  $\cdot\text{OH}$  radical signals (Figure S13, Supporting Information), indicating that DNPs exhibit excellent type I and type II photodynamic therapy effects under specific wavelength laser excitation, capable of generating various reactive oxygen species. This indicates tremendous therapeutic potential for solid tumors, even under hypoxic conditions. Overall, the study results demonstrate that DNPs prepared from the novel A-D-A molecule DTPC-N2F serve as promising candidates for combined PTT, type I PDT, and type II PDT treatments of cancer under near-infrared 980 nm laser irradiation.

### 2.3. In Vitro Antitumor Properties

The in vitro biocompatibility and antitumor therapeutic effects of the DNPs were subsequently evaluated. To ensure the safety of DNPs-based therapy, a preliminary assessment of toxicity was conducted using the cell counting kit-8 (CCK-8) assay after DNPs were incubated with U14 and ncm460 cells. As shown in Figure 4A,B, even at the highest concentration of  $100\ \mu\text{g mL}^{-1}$ , DNPs did not affect cell viability in the absence of laser irradiation, with survival rates for both cell types exceeding 95%, demonstrating excellent biocompatibility and potential for biomedical applications. U14 cells incubated with different concentrations of DNPs were exposed to 980 nm laser irradiation at two different power levels ( $1.0$  and  $0.6\ \text{W cm}^{-2}$  for 4 min). At concentrations of  $12.5$ ,  $25$ , and  $50\ \mu\text{g mL}^{-1}$ , cell viability for both power settings was less than 20% (Figure 4C). Further analysis using a Calcein/PI cell viability/cytotoxicity assay kit assessed live and dead cells in the presence and absence of laser irradiation. In the DNPs+Light(L) and DNPs@CM+L groups, a significant number of dead cells emitting red fluorescence were observed, while the PBS, PBS+L, and DNPs groups showed no significant number of dead cells (Figure 4D). Quantitative analysis of red fluorescence in cells using ImageJ software showed similar results (Figure S14, Supporting Information). These findings indicate that DNPs have an excellent ability to kill tumor cells when excited by 980 nm laser irradiation at certain concentrations.

To further investigate the oxidative damage to cells caused by the strong A-D-A structure of DTPC-N2F and its type I and type II PDT effects, 2,7-dichlorofluorescein diacetate (DCFH-DA) was used as an ROS probe to assess intracellular ROS levels. In the fluorescence images, abundant green fluorescence signals were observed in the cells of the DNPs+L and DNPs@CM+L groups, while the cells in the PBS, PBS+L, and DNPs groups exhibited minimal green fluorescence. Quantitative analysis of 3D images using ImageJ software showed similar results (Figure 4E). Additionally, intracellular ROS levels were quantified by flow cytometry (FCM), revealing ROS levels of 55.36% and 63.70% in the DNPs+L and DNPs@CM+L groups, respectively, which were significantly greater than those in the other groups (Figure 4F). The mechanism of ROS generation is such that when a photosensitizer is activated under light irradiation at a specific wavelength, one of the energy dissipation pathways is through ISC to a relatively stable excited triplet state (T1). During the ISC process, triplet-excited oxygen molecules

are produced, or electron transfer is induced, resulting in the generation of different types of ROS.<sup>[5a,23]</sup> The calculated  $\Delta E_{\text{ST}}$  for DNPs is 0.55 eV, indicating excellent ISC capability. Compared to previously published literature, DNPs demonstrate superior ROS efficiency (Table S2, Supporting Information). Particularly in the DNPs@CM+L group, the DNPs are more easily engulfed due to encapsulation by homologous tumor cell membranes, exhibiting a stronger ability to induce intracellular ROS production.

During PTT and PDT, tumor cells undergo apoptosis, and changes in the mitochondrial membrane potential and nuclear DNA damage are often indicators of cell apoptosis.<sup>[32]</sup> To further explore the mechanisms of cell damage induced by PTT and PDT after DNPs laser irradiation, JC-1 staining was first used to observe changes in the mitochondrial membrane potential. In the DNPs+L and DNPs@CM+L groups, JC-1 existed in a monomeric form in the mitochondrial matrix due to the decrease in the mitochondrial membrane potential, leading to a significant decrease in the red fluorescence intensity within the mitochondria and a significant increase in the green fluorescence intensity in the cytoplasm. In contrast, in the PBS, PBS+L, and DNPs groups, JC-1 aggregated in the mitochondrial matrix, resulting in abundant red fluorescence and very weak green fluorescence (Figure 4G). Quantitative analysis of the fluorescence intensity of JC-1 aggregates and JC-1 monomers also revealed similar results (Figure S15, Supporting Information).  $\gamma$ -H2AX immunofluorescence staining was used to detect DNA damage in U14 cells in the different treatment groups. Significant DNA damage was observed in both the DNPs+L and DNPs@CM+L groups (Figure 4H). Quantitative analysis of the green fluorescence intensity of  $\gamma$ -H2AX also revealed that the fluorescence intensity in the DNPs+L and DNPs@CM+L groups was significantly greater than that in the other three groups (Figure S16, Supporting Information). These two experiments demonstrated that DNPs can induce tumor cell death after 980 nm laser irradiation by inducing changes in the mitochondrial membrane potential and DNA damage. Furthermore, the Annexin V-FITC Apoptosis Detection Kit was used to detect cell apoptosis in the different treatment groups. Increased proportions of early and late apoptotic cells were observed in the DNPs+L and DNPs@CM+L groups, with late apoptotic cells accounting for 44.4% and 47%, respectively, which were significantly greater than those in the other groups (Figure 4I). During phototherapy, the large amount of ROS generated can activate P53, increase the expression of the pro-apoptotic protein Bax, and inhibit the expression of the anti-apoptotic protein Bcl-2. These changes promote the cleavage of caspase-3 into its active form, thereby inducing mitochondrial-mediated apoptosis in tumor cells.<sup>[31b]</sup> Ultimately, our Western blot experiments confirmed that following DNPs-mediated phototherapy, Bax and cleaved caspase 3 expression increased while Bcl-2 expression decreased (Figure 4J). These results indicate that nanoparticles prepared based on the A-D-A-structured DTPC-N2F, which has strong ICT, low bandgap, efficient ISC, and high photothermal conversion efficiency, can produce good PTT and PDT effects under 980 nm laser irradiation. This leads to changes in mitochondrial membrane potential and induction of DNA damage, while also regulating the expression of apoptosis-related proteins, thereby promoting tumor cell death.

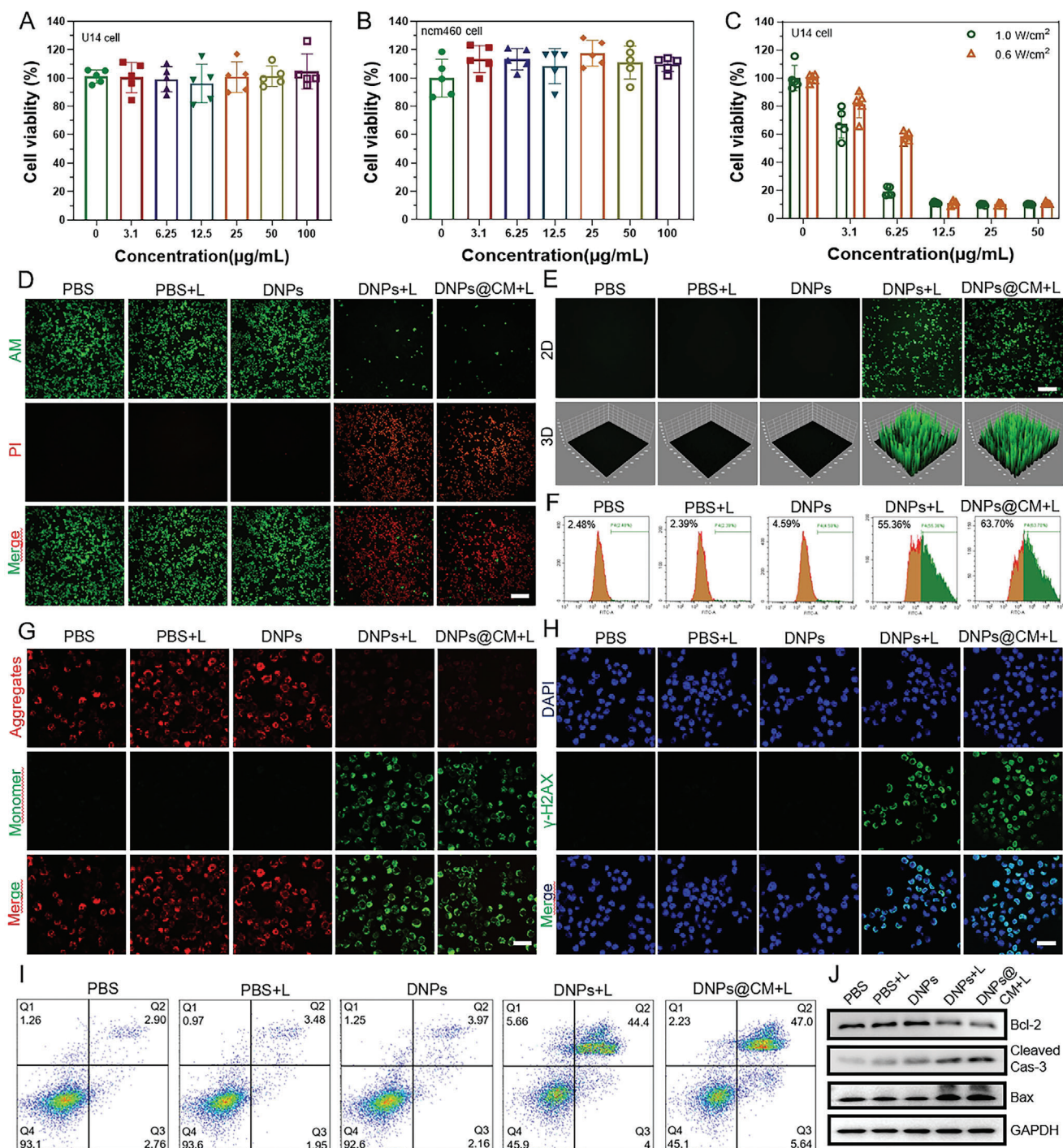


**Figure 4.** In vitro antitumor performance assessment. The impact of different concentrations of DNPs on the viability of U14 cells (A) and ncm460 cells (B) ( $n = 5$ ). C) Effect of different concentrations of DNPs under different power levels of 980 nm laser irradiation on the viability of U14 cells ( $n = 5$ ). D) Fluorescence images of live/dead staining of U14 cells from different treatment groups. Scale bar = 200 µm. Fluorescence images and quantitative analysis of intracellular ROS production in U14 cells from different treatment groups using CLSM (E) and FCM (F). Scale bar = 200 µm. G) Representative CLSM images of JC-1-stained U14 cells showing changes in the mitochondrial membrane potential after different treatments. Scale bar = 50 µm. H) Representative CLSM images of  $\gamma$ -H2AX-stained U14 cells indicating DNA damage after different treatments. Scale bar = 50 µm. I) Cell apoptosis in U14 cells after different treatments determined by Annexin V-FITC/PI staining followed by FCM. J) Apoptosis-related proteins after different treatments. The data are presented as the mean  $\pm$  SD.

#### 2.4. Induction of ICD, Antigen Adsorption, and Dendritic Cells Maturation In Vitro

Research has shown that PTT and PDT can induce ICD in tumors.<sup>[33]</sup> Dead or dying cells release large amounts of tumor antigens and damage-associated molecular patterns (DAMPs), primarily calreticulin (CRT) exposed on the cell membrane surface, and a significant amount of high mobility group box 1 (HMGB1) released into the extracellular environment from the cell nucleus, thereby stimulating the recruitment and maturation of dendritic cells (DC) and promoting antigen presentation.<sup>[34]</sup> In this study, after staining cells with CRT, abundant green fluorescence was observed on the cell membrane in the DNPs+L and DNPs@CM+L groups, while the intensity of green fluorescence was weak in the PBS, PBS+L, and DNPs groups (Figure 5A). Quantitative analysis of green fluorescence also showed similar results (Figure S17, Supporting Information). Similarly, after staining cells with HMGB1, strong green fluorescence was observed on the cell nucleus surface in the PBS, PBS+L, and DNPs groups, while the fluorescence intensity was weaker in the DNPs+L and DNPs@CM+L groups, as shown in Figure 5B. Quantitative analysis revealed similar results (Figure S18, Supporting Information), indicating that PTT and PDT induced the release of HMGB1 expressed in the cell nucleus into the extracellular environment. These findings validate the excellent ability of DNPs-induced PTT and PDT to amplify oxidative stress to promote ICD in tumor cells.

To enhance the synergistic phototherapy and immunotherapy capability of DNPs and increase their sustained induction of ICD in vivo, alum was used in the animal experiments of this study. Aluminum hydroxide, one of the earliest adjuvants approved by the FDA for vaccine production,<sup>[35]</sup> can adsorb antigens and synergistically stimulate DC maturation during phototherapy, thereby enhancing the antitumor immune response.<sup>[36]</sup> The ability of alum to capture antigens was first validated. DLS detection revealed that after coinubation with antigens, the average particle size of alum increased from 458 to 712 nm (Figure 5C; Figure S19, Supporting Information), and the surface charge changed from positive to negative (Figure 5D). Additionally, SDS-PAGE and Coomassie blue staining revealed significant changes in the supernatant after cell lysis, after treatment with alum alone, and after coinubation with the cell lysate (Figure 5E), confirming the strong antigen-capturing ability of alum. The antitumor immune response first requires antigen-presenting cells (APC) recognition, processing, and antigen presentation, with DC maturation playing a crucial role in adaptive immunity.<sup>[37]</sup> To verify the ability of alum to stimulate DC maturation, a Transwell coculture system was used to coculture tumor cells and DC (Figure 5F). FCM revealed that the maturity of DC (CD11c<sup>+</sup> CD80<sup>+</sup> CD86<sup>+</sup>) increased significantly in the DNPs+L+Alum group, reaching 87.4%, compared to that in the PBS group (34.7%) and DNPs group (35.6%), with 47.1% and 73.6%, respectively, in the DNPs+L group and the Alum group (Figure 5G; Figure S20, Supporting Information). In summary, under 980 nm laser irradiation, DNPs effectively exposed tumor-associated antigen (TAA), while alum demonstrated the ability to capture antigens and stimulate DC maturation.

#### 2.5. In Vivo Antitumor Performance

In previous experiments, we separately validated the PTT and PDT effects of DNPs under 980 nm laser irradiation. Additionally, we confirmed the ability of alum to stimulate antigen adsorption and DC maturation, with previous literature supporting its application in animal tumor therapy.<sup>[35a,36a]</sup> In subsequent experiments, to assess the therapeutic efficacy of cervical cancer treatment in vivo, we constructed a more clinically relevant mouse model of cervical cancer and used intravaginally in situ treatment (Figure 6A). After the cervical tumors developed locally, the bioluminescence intensity was examined using a small animal live imaging system, and when it reached  $1 \times 10^6$  photons (p) s<sup>-1</sup> cm<sup>-2</sup> sr<sup>-1</sup>, the mice were randomly divided into six groups ( $n = 5$ ): PBS, PBS+L, DNPs@CM, Alum, DNPs@CM+L, and DNPs@CM+Alum+L. Each mouse in these groups received treatment on the 1st and 5th days. Tumor growth was monitored using live animal imaging during this period. On the 10th day, the mice were euthanized, and their dissected organs were examined. The live imaging results showed no significant therapeutic effects in the PBS, PBS+L, DNPs@CM, or Alum groups, whereas noticeable tumor shrinkage was observed in the DNPs@CM+L and DNPs@CM+Alum+L groups; this effect was particularly evident, with complete disappearance of tumors in 5 mice in the DNPs@CM+Alum+L group. Similar results were observed in the corresponding anatomical images of the reproductive organs of the mice (Figure 6B). After the mice were dissected, the volume of cervical tumors and the fluorescence intensity of bioluminescence imaging on the 10th day were measured. Significant differences were observed between the DNPs@CM+L, DNPs@CM+Alum+L, and other groups. The addition of alum led to the best therapeutic efficacy in the DNPs@CM+Alum+L group (Figure 6C,D). Furthermore, continuous observation of the body weights of the mice throughout the treatment period revealed no significant changes (Figure 6E).

#### 2.6. In Vivo Immunological Effect of Photoimmunotherapy

Pathological sections of cervical tumor tissues stained with H&E revealed extensive tumor cell apoptosis and necrosis in the DNPs@CM+L and DNPs@CM+Alum+L groups (Figure 7A). Terminal deoxynucleotidyl transferase dUTP Nick End Labeling (TUNEL) fluorescence staining revealed extensive red fluorescence, which was particularly evident in the DNPs@CM+Alum+L group (Figure 7B,C; Figure S21, Supporting Information). These experiments demonstrated the excellent in vivo antitumor therapeutic effects of DNPs under 980 nm laser irradiation. Coadministration of alum-induced persistent ICD due to its antigen adsorption and ability to stimulate DC maturation, thereby exhibiting superior antitumor efficacy.

To validate the ability of DNPs combined with alum to induce DC maturation and activate effector T cells in vivo under 980 nm laser excitation, FCM was used to analyze the expression of T cells and DC in tumors. Compared to those in the PBS group, the number of T cells in the DNPs@CM+L and DNPs@CM+Alum+L groups significantly increased, with the percentage of CD8<sup>+</sup> T cells increasing from 0.92% to 6.84% and 7.93%, respectively, and the percentage of CD4<sup>+</sup> T

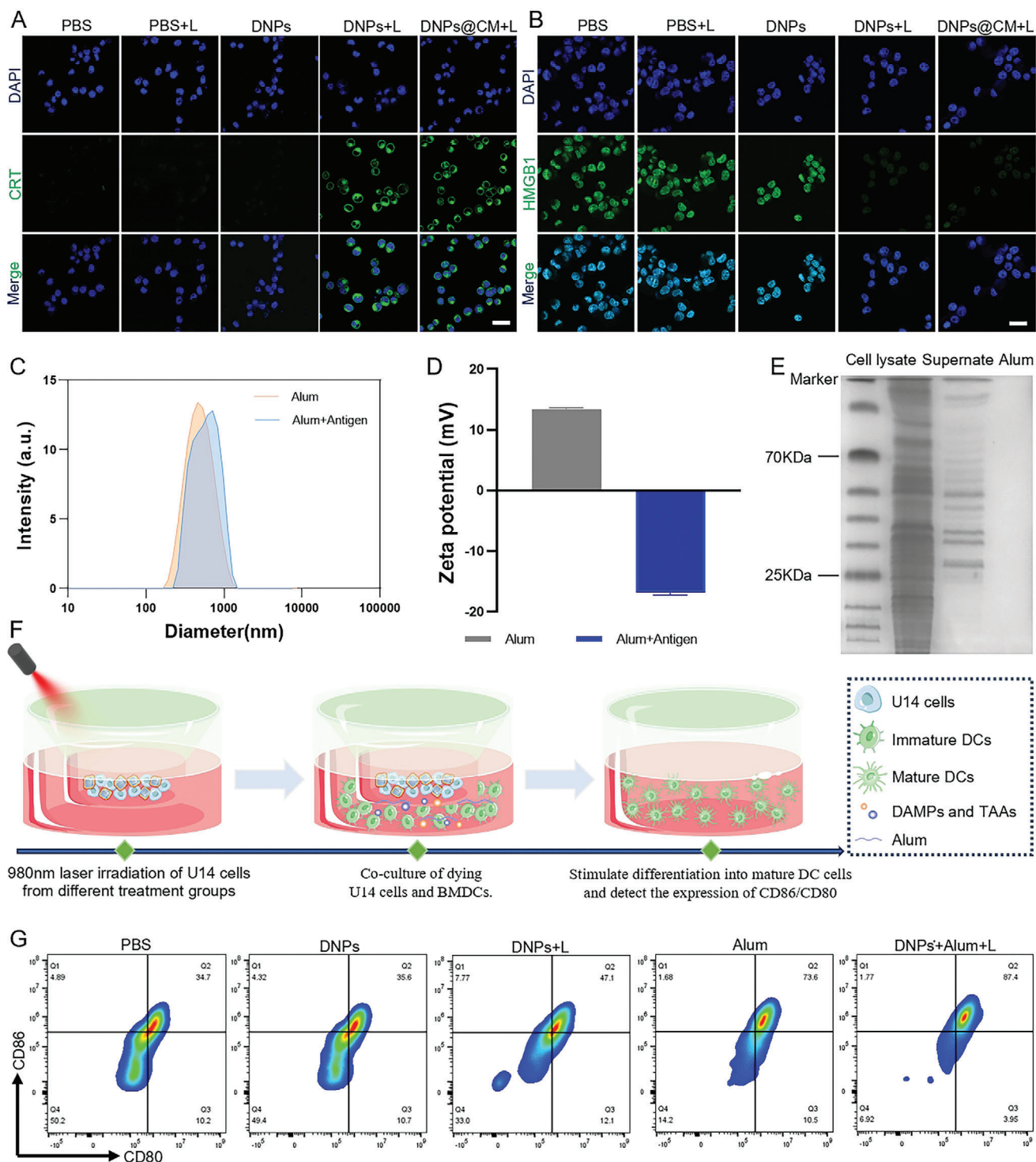


**Figure 5.** Induction of ICD and study of antigen adsorption and stimulation of DC maturation. A) Representative CLSM images of U14 cells showing CRT exposure in different treatment groups. Scale bar = 50  $\mu\text{m}$ . B) Representative CLSM images of U14 cells showing HMGB1 release in different treatment groups. Scale bar = 50  $\mu\text{m}$ . C) Changes in the hydrated particle size of alum before and after antigen adsorption detected by DLS. D) Zeta potential changes of alum before and after antigen adsorption. E) Changes in SDS-PAGE and Coomassie blue staining bands of antigens before and after adsorption on alum. F) Simplified schematic diagram of the Transwell coculture system. G) FCM analysis of the effect of different treatments on DC maturation.

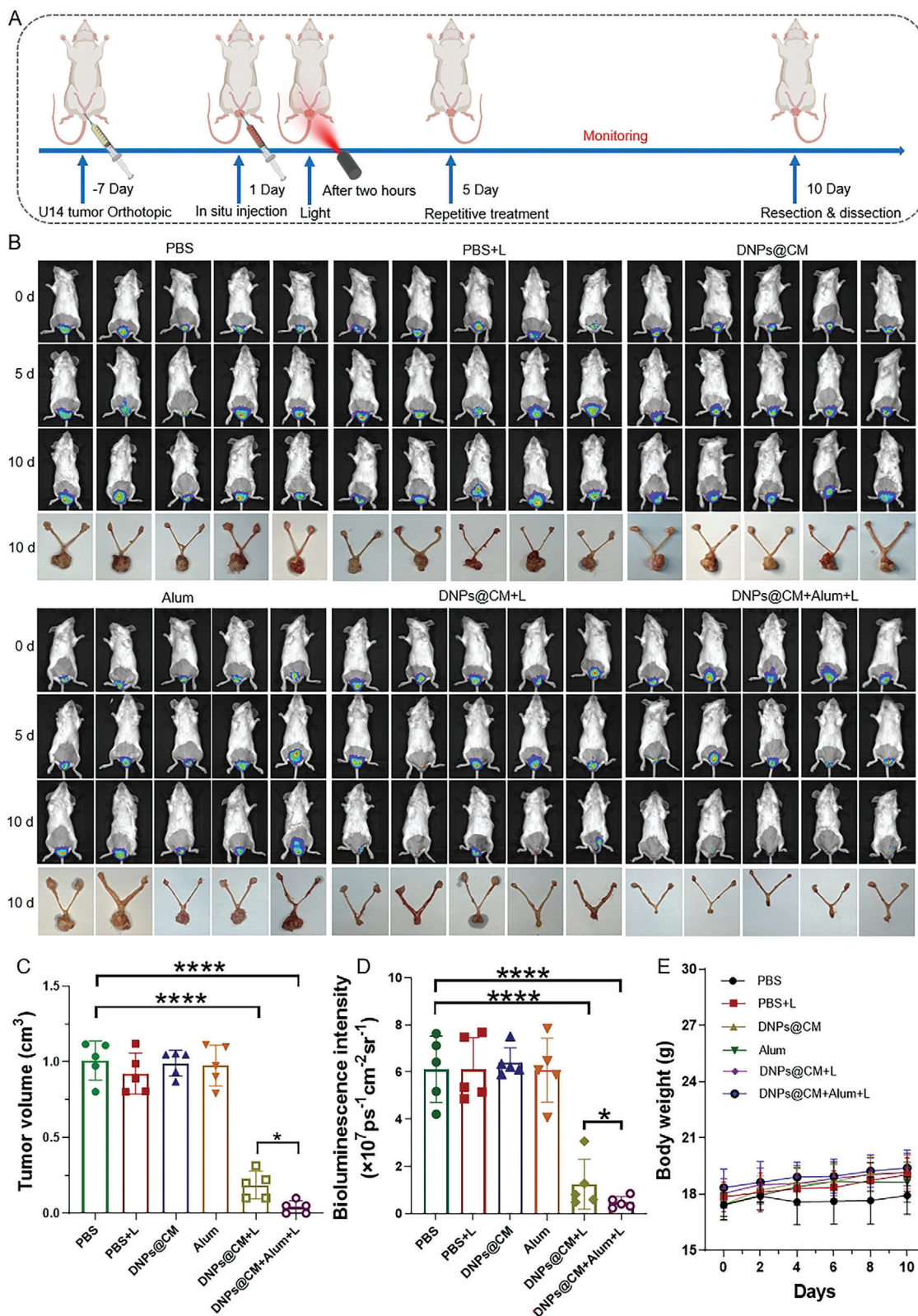


**Figure 6.** In vivo evaluation of antitumor effects. A) Schematic diagram of in vivo treatment. B) Bioluminescence images and anatomical images of the reproductive systems of mice in different treatment groups. C) Tumor volumes at the end of treatment in different treatment groups ( $n = 5$ ). D) Quantitative analysis of bioluminescence images at the end of treatment in different treatment groups ( $n = 5$ ). E) Changes in mouse body weight during treatment ( $n = 5$ ). The data are presented as the mean  $\pm$  SD. The  $p$  values were calculated using one-way analysis of variance (ANOVA),  $*p < 0.05$ ,  $**p < 0.01$ , and  $***p < 0.001$ .

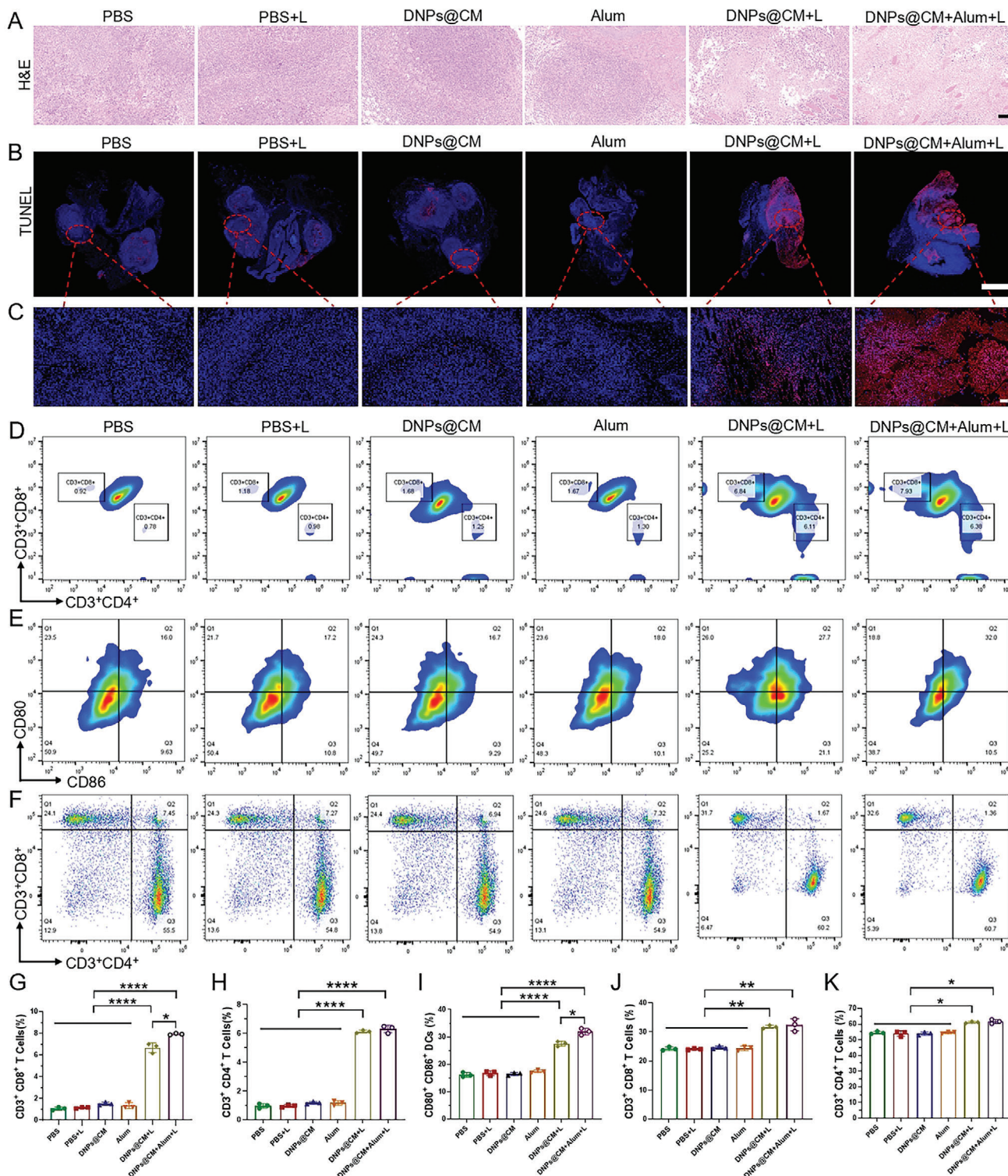


**Figure 7.** Pathological sections and immune effect evaluation after in vivo treatment. A) H&E staining images of tumors in different treatment groups; scale bar = 50  $\mu$ m. B) TUNEL staining images of tumors in different treatment groups, Scale bar = 1000  $\mu$ m. C) Scale bar = 50  $\mu$ m). D) FCM analysis and quantification G, H) of tumor-infiltrating CD8<sup>+</sup> T cells (CD3<sup>+</sup> CD8<sup>+</sup>) and CD4<sup>+</sup> T cells (CD3<sup>+</sup> CD4<sup>+</sup>) in different treatment groups ( $n = 3$ ). E) FCM analysis and quantification I) of tumor-infiltrating DC (CD80<sup>+</sup> CD86<sup>+</sup>) in different treatment groups ( $n = 3$ ). F) FCM analysis and quantification (J, K) of CD8<sup>+</sup> T cells (CD3<sup>+</sup> CD8<sup>+</sup>) and CD4<sup>+</sup> T cells (CD3<sup>+</sup> CD4<sup>+</sup>) in the spleens of different treatment groups ( $n = 3$ ). The data are presented as the mean  $\pm$  SD. The  $p$  values were calculated using two-tailed unpaired t-tests or one-way ANOVA, \* $p < 0.05$ , \*\* $p < 0.01$ , and \*\*\* $p < 0.001$ .

cells increasing from 0.78% to 6.11% and 6.38%, respectively (Figure 7D,G,H, Figure S22, Supporting Information). The activation of effector T-cell function is related to DC maturation. Therefore, when targeting DC labeled with antibodies against CD11c<sup>+</sup>, CD80<sup>+</sup>, and CD86<sup>+</sup>, FCM revealed a significant increase in the percentage of mature DCs (CD80<sup>+</sup> CD86<sup>+</sup>) in the DNPs@CM+L and DNPs@CM+Alum+L groups compared to that in the PBS group, increasing from 16% to 27.7% and 32%, respectively (Figure 7E,I, Figure S23, Supporting Information). The T cell content in the spleen was also studied. Compared to those in the PBS group, the numbers of CD8<sup>+</sup> and CD4<sup>+</sup> T cells in the DNPs@CM+L and DNPs@CM+Alum+L groups increased (Figure 7F,J,K, Figure S24, Supporting Information). These results demonstrate that in mice, PTT and PDT induced by DNPs via 980 nm laser irradiation combined with the immune adjuvant alum can induce DC maturation, further promoting the activation of effector T cells. This synergistic effect of phototherapy and immunotherapy plays a therapeutic role in cervical cancer treatment. To further validate the biocompatibility of DNPs in animal treatment, all mice were dissected after the termination of treatment. Important organs, such as the heart, liver, spleen, lungs, and kidneys, were collected for H&E staining, and blood samples were taken for complete blood analysis and liver and kidney function and biochemical analysis. No abnormalities were detected (Figures S25 and S26, Supporting Information), indicating that the use of DNPs as the main material for animal treatment is safe and has no significant adverse effects on the overall health of the mice.

### 2.7. Antitumor Metastasis of DNPs-Based Photoimmunotherapy

ICD can induce the activation of memory T cells, thereby inhibiting the growth of metastatic tumors.<sup>[38]</sup> To further investigate the inhibitory effect of DNPs-based phototherapy combined with alum on metastatic tumors, we simulated the clinical process by constructing an in situ cervical cancer and cervical cancer intraperitoneal metastasis model (Figure 8A). The mice were treated on the 1st and 5th days, and on the 14th day, they were euthanized for observation of the growth of primary and metastatic tumors. Due to the occurrence of ascites caused by intraperitoneal metastases, changes in ascite volume were also observed. In the PBS group, large cervical local tumors were observed to grow toward the uterus, accompanied by numerous intraperitoneal metastatic lesions (dense metastatic lesions visible in the mesentery) and large metastatic lesions (the lower edge of the liver), along with significant bloody ascites. Compared to the PBS group, the DNPs@CM+Alum+L group showed fewer intraperitoneal metastatic lesions and fewer ascites while eliminating cervical cancer lesions (Figure 8B,E). The inhibition of metastatic tumors is related to the continuous induction of ICD by phototherapy combined with adjuvants, which leads to the activation of memory T cells and the triggering of immune memory and more sustained protection.<sup>[39]</sup> On day 14 of treatment, the numbers of effector memory T cells (Tems, CD44<sup>+</sup> CD62L<sup>-</sup>) and central memory T cells (Tcms, CD44<sup>+</sup> CD62L<sup>+</sup>) in the spleen were analyzed. The proportions of CD44<sup>+</sup> CD62L<sup>-</sup> T cells and CD44<sup>+</sup> CD62<sup>+</sup> T cells in the DNPs@CM+Alum+L group were greater than those in the PBS group (Figure 8C,F,G; Figure S27, Sup-

porting Information). An increase in CD44<sup>+</sup> cell expression was also observed in CD8<sup>+</sup> T cells in tumor tissues (Figure 8D,H; Figure S28, Supporting Information). These results indicate that the immune memory induced by DNPs@CM+Alum+L is the strongest, thus exerting a certain degree of inhibitory effect on intraperitoneal metastasis and ascites production. The above results confirmed that the DNPs induced PTT and PDT effects in vivo under 980 nm laser excitation. In combination with alum, they can induce persistent ICD, exhibit synergistic antitumor therapeutic effects, promote immune memory, enhance systemic antitumor immune responses, and inhibit the growth of intraperitoneal metastatic tumors.

### 3. Conclusion

In summary, we developed a novel A-D-A small molecule, DTPC-N2F, which can be excited by long-wavelength NIR light and possesses a high molar extinction coefficient. Its unique molecular structure endows it with a narrow bandgap and excellent ISC capability. Using nanoprecipitation strategy, DTPC-N2F was encapsulated in DSPE-PEG5000 nanoparticles to form DNPs, resulting in a noticeable redshift in the light absorption spectrum. Under 980 nm laser excitation, DNPs achieved deep tissue penetration and demonstrated high photothermal conversion efficiency ( $\eta = 67.94\%$ ), excellent PTT, type I and type II PDT functions (facilitating <sup>1</sup>O<sub>2</sub>, ·O<sub>2</sub><sup>-</sup> and ·OH generation), along with good biocompatibility. In vitro experiments demonstrated that phototherapy induced changes in the mitochondrial membrane potential, DNA damage, and apoptotic markers expression, promoting cell apoptosis. To enhance the orthotopic cervical cancer-targeting ability, we extracted tumor cell membranes for encapsulating DNPs to form DNPs@CM. Given its unique physiological characteristics, we proposed a noninvasive therapy strategy for cervical cancer coupling A-D-A nanoaggregates with optical fiber intervention technology. Its effectiveness has been proved in an orthotopic cervical cancer animal model, offering new insights for clinical early-stage cervical cancer treatment. Cancer metastasis is the leading cause of cancer-related deaths. In combination with clinical aluminum adjuvant gel, a novel photoimmunotherapy strategy for cervical cancer was developed, leveraging efficient phototherapy-induced immunogenic cell death and immune adjuvants to construct an in-situ tumor vaccine. This approach activates the body's anti-tumor immune response, including promoting the maturation of DC and stimulating the differentiation of memory T cells, effectively suppressing cervical cancer metastasis. Its effectiveness has been proved in an intraperitoneal metastasis animal model. The noninvasive therapy strategy, which combines A-D-A structured nanoaggregates and aluminum adjuvant gel with optical fiber intervention technology, demonstrates high efficiency, safety, and convenience. This approach provides new insights for treating both early-stage and advanced cervical cancer clinically.

### 4. Experimental Section

*Synthesis of DTPC-N2F:* DTPC-N2F-CHO (138 mg, 0.1 mmol) and 2-(6,7-difluoro-3-oxo-2,3-dihydro-1H-cyclopenta[b]naphthalen-1-ylidene) malononitrile (68 mg, 0.24 mmol) were dissolved in toluene (10 mL).

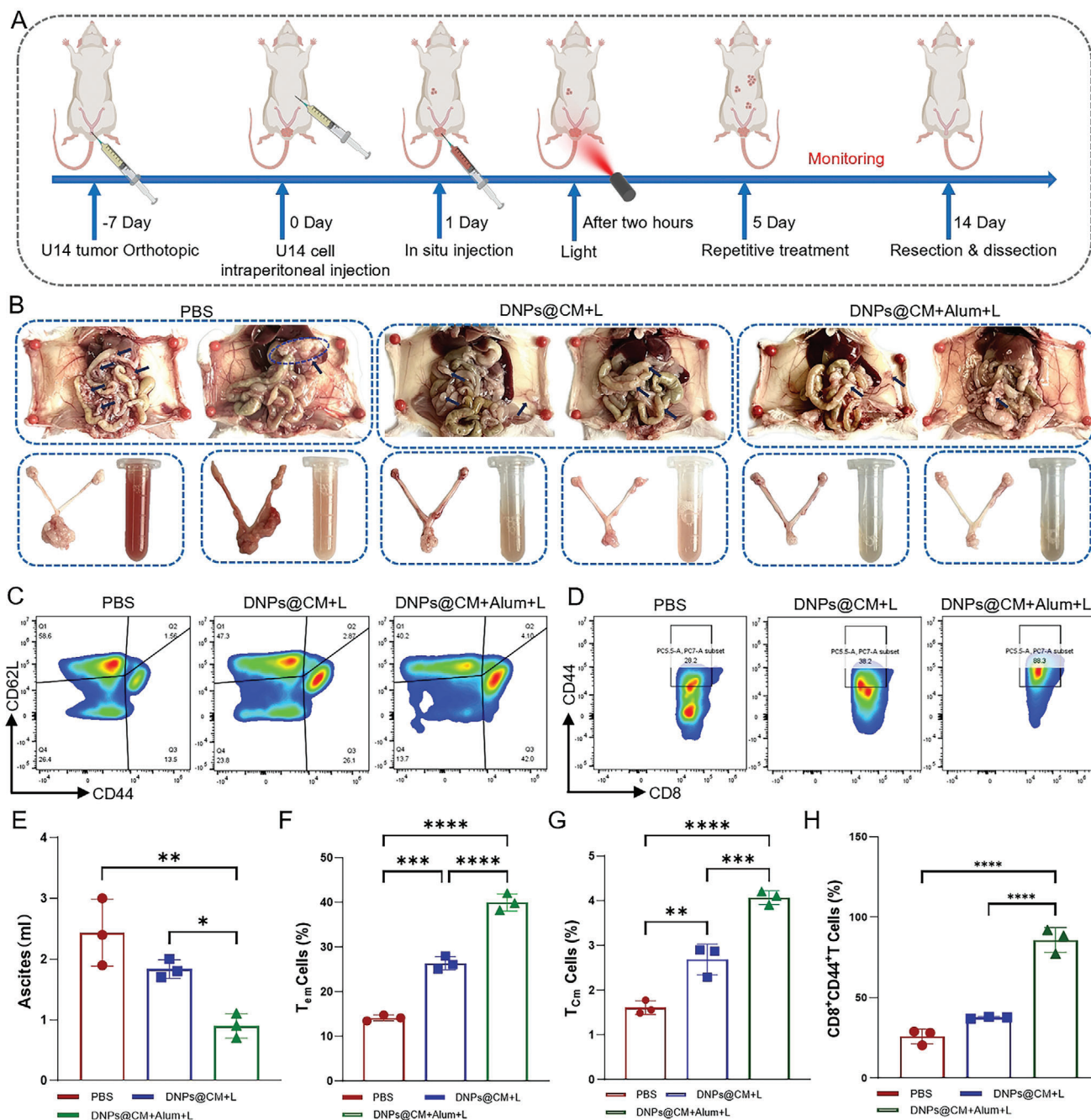


**Figure 8.** Analysis of immune memory and suppression of intraperitoneal metastases. A) Schematic diagram illustrating the construction of intraperitoneal metastases and in vivo treatment. B) Analysis of the suppression of intraperitoneal metastasis and ascites volume after treatment of cervical tumors, with statistical analysis of ascites volume E). C) FCM analysis and quantification F, G) of memory cells in the spleen (CD3<sup>+</sup> CD8<sup>+</sup> CD44<sup>+</sup> CD62L<sup>-</sup> and CD3<sup>+</sup> CD8<sup>+</sup> CD44<sup>+</sup> CD62L<sup>+</sup>) ( $n = 3$ ). D) FCM analysis and quantification H) of tumor-infiltrating memory T cells (CD3<sup>+</sup> CD8<sup>+</sup> CD44<sup>+</sup>) ( $n = 3$ ). The data are presented as the mean  $\pm$  SD. The  $p$  values were calculated using two-tailed unpaired t-tests or one-way ANOVA, \* $p < 0.05$ , \*\* $p < 0.01$ , and \*\*\* $p < 0.001$ .

BF<sub>3</sub>•OEt<sub>2</sub> (0.3 mL) and acetic anhydride (0.3 mL) were added, and the reaction mixture was stirred at room temperature for 15 min. Then, the reaction mixture was added dropwise to methanol with stirring. The precipitate was purified by chloroform on silica gel to yield a brown solid as the desired product DTPC-N2F (152 mg, 80% yield).

**Synthesis of DNP:** Preparation of DNP through nanoprecipitation:<sup>[40]</sup> First, DTPC-N2F (0.5 mg) and DSPE-PEG 5000 (20 mg) were each dissolved in 1 mL of THF, and after sonication for uniform mixing, the mixture was rapidly added to 10 mL of THF solution (THF to water ratio of 1:9) and sonicated for 20 min in a water bath. The solution was then left on a shaker overnight to allow the THF to evaporate.

The solution was filtered through a 0.45  $\mu\text{m}$  pore filter, followed by three rounds of centrifugal ultrafiltration using a Millipore filter to remove THF and impurities, and the supernatant was collected. The resultant DNPs formed a brown-red liquid. The concentration of the samples was remeasured according to the standard curve to confirm the actual content.

**Extraction of the Tumor Cell Membrane and Preparation of DNPs@CM:** U14 cells were cultured in a 10 cm dish until they reached a confluence of greater than 80%. After digestion and centrifugation, the cells were resuspended in 1 ml of PBS and stored on ice for 20 min. Subsequently, the cells were subjected to multiple freeze–thaw cycles—freezing in liquid nitrogen followed by thawing in a 37 °C water bath—3–5 times. The resulting cell suspension was centrifuged at 1000 rpm for 3 min to remove the precipitate and retain the supernatant. The supernatant was then centrifuged at 18 000 rpm for 60 min, and the supernatant was discarded while the precipitate, representing the cell membrane, was resuspended in 0.5 mL of distilled water. The protein content was quantified using a standard curve, and the cell membrane was mixed with DNPs at a 1:1 ratio. The mixture was sonicated for 10 min in an ultrasonic water bath to encapsulate the tumor cell membrane and obtain DNPs@CM.

**Animal Study:** This study utilized female BALB/c mice aged 6–8 weeks and weighing 15–18 grams. All animal experiments were approved by the Animal Ethics Committee of Tianjin University (Tianjin, China) under approval number TJUE-2024-315 and were conducted in accordance with the Tianjin University Guidelines for the Care and Use of Laboratory Animals. The mice were housed under standard specific pathogen-free conditions with ad libitum access to food and water. The environmental conditions were maintained at a temperature of 23–26 °C, humidity of 40%–60%, and a 12-h light/dark cycle, with 3–4 mice per cage. At the conclusion of the study, euthanasia was performed by cervical dislocation following inhalation anesthesia.

**Antitumor Therapy Efficacy:** After establishing the orthotopic cervical cancer mouse model, the growth of cervical tumors was monitored using a small animal live imaging system. The maximum tumor volume was set to 1500  $\text{mm}^{-3}$  for this experiment. Mice were anesthetized with isoflurane, and each mouse received an intraperitoneal injection of D-luciferin potassium salt (100  $\mu\text{L}$ , 10  $\text{mg mL}^{-1}$ ). The bioluminescence intensity of the tumors was examined. Treatment was initiated on the 7th day after tumor cell inoculation (Day 1), and the mice were randomly divided into six groups ( $n = 5$ ): PBS, PBS+L, DNPs@CM, Alum, DNPs@CM+L, and DNPs@CM+Alum+L. The dose of DNPs was 1  $\text{mg k}^{-1}\text{g}$ , and the dose of alum was 5  $\text{mg k}^{-1}\text{g}$ , with a total volume of 100  $\mu\text{L}$  per group. Intratumoral injection was performed for orthotopic cervical cancer tumors. Two hours after drug injection, the method of transvaginal intervention using a 980 nm laser with a power of 0.6  $\text{W cm}^{-2}$  to irradiate the tumor for 4 min as a therapeutic treatment. Repeated treatments were administered on the 5th day. During the treatment period, tumor growth was monitored based on bioluminescence using a small animal imaging system, and mouse weights were recorded every two days. Bioluminescent images on the 10th day of treatment were analyzed using Living Image software. On the 10th day of treatment, the mice were euthanized, and their reproductive systems were dissected for measurement of cervical tumor size and analysis. Hematoxylin and eosin (H&E) staining and Terminal deoxynucleotidyl transferase dUTP Nick End Labeling (TUNEL) staining were performed on the tumors.

**Evaluation of the Immune Response In Vivo:** On the 10th day posttreatment, the mice were euthanized, and the tumor tissues were dissected for analysis of the T-cell and DC contents via FCM. Additionally, the spleen was excised to measure the T-cell content. The experimental procedure was briefly described as follows: Excised tumors were enzymatically digested using DNase I and type IV collagenase for 1 h and filtered through a 70  $\mu\text{m}$  filter, and single-cell suspensions were prepared using red blood cell lysis buffer. The collected DCs and T cells were stained with fluorescently labeled monoclonal antibodies (against CD45, CD3, CD4, CD8a, CD11c, CD80, and CD86) at 4 °C, followed by FCM. The excised spleen was directly processed into single-cell suspensions using red blood cell lysis buffer, and the collected T cells were stained with fluorescently labeled monoclonal antibodies at 4 °C for FCM.

**Intraperitoneal Metastasis Model Construction, Treatment Efficacy, and Immunological Evaluation:** To simulate the clinical behavior of cervical cancer, after establishing the orthotopic cervical cancer mouse model as described above, intraperitoneal tumor seeding was performed 6 days after the inoculation of tumor cells. Mice were first anesthetized with isoflurane, and the abdomen was disinfected using alcohol swabs. A 1 ml of PBS solution containing  $1.5 \times 10^6$  U14-LUC cells was injected into the peritoneal cavity. On the 7th day (day 1 of treatment), the mice were randomly divided into three groups ( $n = 3$ ): PBS, DNPs@CM+L, DNPs@CM+Alum+L. Drugs were injected into the cervical tumor at a dose of 1  $\text{mg k}^{-1}\text{g}$  and an alum dosage of 5  $\text{mg k}^{-1}\text{g}$ , totaling 100  $\mu\text{L}$  per group. Two hours after drug injection, the tumors were irradiated with a 980 nm laser for 4 min at a power of 0.6  $\text{W cm}^{-2}$  on days 1 and 5 of treatment. Abdominal distension of the mice was observed during the treatment period. On day 14 of treatment, the mice were euthanized, and the reproductive system and abdominal cavity of the mice were dissected. Peritoneal fluid was collected and measured, and the presence of tumor metastasis on abdominal organs and peritoneal surfaces was observed. Tumors and spleens were collected for FCM of memory T cells and stained with the fluorescently labeled monoclonal antibodies CD44 and CD62L.

**Statistical Analysis:** The experiments described above were repeated three times. The sample sizes were presented in the figures and tables. The data were expressed as the mean  $\pm$  standard deviation. Two-group comparisons were conducted using the t-test, while a one-way analysis of variance (ANOVA) was used for comparisons among multiple groups. GraphPad Prism 9 and Origin software were used for data analysis and graphical presentation. Statistical significance was defined as  $p < 0.05$ . Asterisks (\*) denote significance levels as follows: \* $p < 0.05$ , \*\* $p < 0.01$ , and \*\*\* $p < 0.001$ .

## Supporting Information

Supporting Information is available from the Wiley Online Library or from the author.

## Acknowledgements

G.N., X.B., and Y.K. contributed equally to this work. This study was financially supported by grants from the National Natural Science Foundation of China (Grant No. 32071322), National Natural Science Funds for Excellent Young Scholars (Grant No. 32122044), and Technology & Innovation Commission of Shenzhen Municipality (Grant No. JCYJ20210324113004010). The Key Project of Medical Science and Technology Tackling in Henan Province (Grant No. SBGJ202102016) and Science and Technology Tackling in Henan Province (Grant No. 242102310359)

## Conflict of Interest

The authors declare no conflict of interest.

## Data Availability Statement

The data that support the findings of this study are available in the supplementary material of this article.

## Keywords

Acceptor–donor–acceptor molecule, immunogenic cell death, photodynamic therapy, photoimmunotherapy, photothermal therapy

Received: May 20, 2024  
Revised: July 25, 2024  
Published online:

- [1] F. Bray, M. Laversanne, H. Y. A. Sung, J. Ferlay, R. L. Siegel, I. Soerjomataram, A. Jemal, *Ca-Cancer J. Clin.* **2024**, *74*, 229.
- [2] K. S. Tewari, B. J. Monk, *Lancet* **2024**, *403*, 1310.
- [3] a) Z. Zhang, Y. Du, X. Shi, K. Wang, Q. Qu, Q. Liang, X. Ma, K. He, C. Chi, J. Tang, B. Liu, J. Ji, J. Wang, J. Dong, Z. Hu, J. Tian, *Nat. Rev. Clin. Oncol.* **2024**, *21*, 449; b) M. Overchuk, R. A. Weersink, B. C. Wilson, G. Zheng, *ACS Nano* **2023**, *17*, 7979; c) L. X. Lv, B. L. Fan, X. R. Ji, Y. X. Liu, T. Chen, Y. L. Li, X. Y. Gao, P. Chen, B. Tang, G. Chen, *Coordin. Chem. Rev.* **2024**, *507*, 215733; d) X. Wang, J. Qian, Z. Yang, Y. Song, W. Pan, Y. Ye, X. Qin, X. Yan, X. Huang, X. Wang, M. Gao, Y. Zhang, *Adv. Mater.* **2024**, *36*, 2310964.
- [4] F. Ding, J. Liu, K. Ai, C. Xu, X. Mao, Z. Liu, H. Xiao, *Adv. Mater.* **2024**, *36*, 2306419.
- [5] a) P. Agostinis, K. Berg, K. A. Cengel, T. H. Foster, A. W. Girotti, S. O. Gollnick, S. M. Hahn, M. R. Hamblin, A. Juzeniene, D. Kessel, M. Korbelik, J. Moan, P. Mroz, D. Nowis, J. Piette, B. C. Wilson, J. Golab, *Ca-Cancer J. Clin.* **2011**, *61*, 250; b) P. Mroz, A. Yaroslavsky, G. B. Kharkwal, M. R. Hamblin, *Cancers* **2011**, *3*, 2516; c) W. J. Zhang, Y. X. Lv, F. J. Huo, Y. Yun, C. X. Yin, *Adv. Mater.* **2024**, *36*, 2314021.
- [6] a) J. C. Li, D. Cui, J. G. Huang, S. S. He, Z. B. Yang, Y. Zhang, Y. Luo, K. Y. Pu, *Angew. Chem., Int. Ed.* **2019**, *58*, 12680; b) Z. Wang, T. You, Q. Su, W. Deng, J. Li, S. Hu, S. Shi, Z. Zou, J. Xiao, X. Duan, *Adv. Mater.* **2023**, *35*, 2307193.
- [7] a) Y. Tang, H. K. Bisoyi, X.-M. Chen, Z. Liu, X. Chen, S. Zhang, Q. Li, *Adv. Mater.* **2023**, *35*, 2300232; b) W. R. Kang, Y. W. Liu, W. P. Wang, *Acta Pharm. Sin. B* **2023**, *13*, 2346; c) L. Tang, A. N. Zhang, Z. Y. Zhang, Q. Q. Zhao, J. Li, Y. J. Mei, Y. Yin, W. Wang, *Cancer Commun* **2022**, *42*, 141.
- [8] L. Luo, H. Zhou, S. Wang, M. Pang, J. Zhang, Y. Hu, J. You, *Small* **2023**, *19*, 2207694.
- [9] a) H. Zhang, Z. Mao, Y. Kang, W. Zhang, L. Mei, X. Ji, *Coord. Chem. Rev.* **2023**, *475*, 214897; b) G. Feng, G.-Q. Zhang, D. Ding, *Chem. Soc. Rev.* **2020**, *49*, 8179.
- [10] H. Li, Y. Kim, H. Jung, J. Y. Hyun, I. Shin, *Chem. Soc. Rev.* **2022**, *51*, 8957.
- [11] R. V. Huis In 't Veld, J. Heuts, S. Ma, L. J. Cruz, F. A. Ossendorp, M. J. Jager, *Pharmaceutics* **2023**, *15*.
- [12] a) X. S. Li, J. F. Lovell, J. Yoon, X. Y. Chen, *Nat. Rev. Clin. Oncol.* **2020**, *17*, 657; b) G. Niu, H. Wang, Y. Zhai, B. Zhou, Y. Kang, Z. Pei, X. Ji, *Nano Today* **2024**, *56*, 102286.
- [13] M. S. Baptista, J. Cadet, P. Di Mascio, A. A. Ghogare, A. Greer, M. R. Hamblin, C. Lorente, S. C. Nunez, M. S. Ribeiro, A. H. Thomas, M. Vignoni, T. M. Yoshimura, *Photochem. Photobiol.* **2017**, *93*, 912.
- [14] E. Pang, S. Zhao, B. Wang, G. Niu, X. Song, M. Lan, *Coord. Chem. Rev.* **2022**, *472*, 214780.
- [15] a) L. Li, X. Han, M. F. Wang, C. L. Li, T. Jia, X. H. Zhao, *Chem. Eng. J.* **2021**, *417*, 128844; b) H. U. Kim, T. Kim, C. Kim, M. Kim, T. Park, *Adv. Funct. Mater.* **2023**, *33*, 2208082.
- [16] K. Song, X. Su, W. Zhao, F. Ai, A. Umar, S. Baskoutas, *Chem. Eng. J.* **2024**, *485*, 150067.
- [17] B. M. Vickerman, E. M. Zywoot, T. K. Tarrant, D. S. Lawrence, *Nat. Rev. Chem.* **2021**, *5*, 816.
- [18] J. C. Li, S. Q. Wang, F. Fontana, C. Tapeinos, M. A. Shahbazi, H. J. Han, H. A. Santos, *Bioact. Mater.* **2023**, *23*, 471.
- [19] a) X. Wan, C. Li, M. Zhang, Y. Chen, *Chem. Soc. Rev.* **2020**, *49*, 2828; b) P. Li, W. Xiong, J. Wang, J. Hao, M. Li, B. Wang, Y. Chen, W. Si, H. Ren, G. Li, Y. Chen, J. Lü, H. Zhang, C. Jia, X. Guo, *Adv. Mater.* **2023**, *35*, 2301876.
- [20] a) Z. Y. Yao, X. J. Wan, C. X. Li, Y. S. Chen, *Accounts Mater. Res.* **2023**, *4*, 772; b) Z. He, L. Zhao, Q. Zhang, M. Chang, C. Li, H. Zhang, Y. Lu, Y. Chen, *Adv. Funct. Mater.* **2020**, *30*, 1910301.
- [21] a) Y. L. Zhu, H. J. Lai, H. Guo, D. L. Peng, L. Han, Y. Gu, Z. X. Wei, D. K. Zhao, N. Zheng, D. H. Hu, L. Xi, F. He, L. L. Tian, *Angew. Chem., Int. Ed.* **2022**, *61*, e202117433; b) K.-X. Teng, D. Zhang, B.-K. Liu, Z.-F. Liu, L.-Y. Niu, Q.-Z. Yang, *Angew. Chem., Int. Ed.* **2024**, *63*, e202318783.
- [22] H. B. Chen, Z. Zhang, P. R. Wang, Y. X. Zhang, K. Q. Ma, Y. Lin, T. A. Duan, T. F. He, Z. F. Ma, G. K. Long, C. X. Li, B. Kan, Z. Y. Yao, X. J. Wan, Y. S. Chen, *Energ. Environ. Sci.* **2023**, *16*, 1773.
- [23] D. L. Sai, J. Lee, D. L. Nguyen, Y.-P. Kim, *Exp. Mol. Med.* **2021**, *53*, 495.
- [24] Z. Hu, L. Feng, P. Yang, *Adv. Funct. Mater.* **2024**, *34*, 2310818.
- [25] F. Wan, H. Wang, Y. Gu, G. Fan, S. Hou, J. Yu, M. Wang, F. He, L. Tian, *Chemistry* **2024**, *30*, e202303502.
- [26] a) M. Ding, Z. Zhang, N. Yu, J. Zhou, L. Zhu, X. Wang, J. Li, *Adv. Mater.* **2023**, *35*, 2302508; b) S. Li, Q. Deng, Y. Zhang, X. Li, G. Wen, X. Cui, Y. Wan, Y. Huang, J. Chen, Z. Liu, L. Wang, C.-S. Lee, *Adv. Mater.* **2020**, *32*, 2001146; c) X. Meng, Y. Han, S. Wang, X. Wang, Z. Zhang, S. Yao, X. Wan, Z. Liu, Z. Ge, L. Li, *Nano Today* **2023**, *53*, 102030.
- [27] R. Wang, R. Xiao, Z. Zeng, L. Xu, J. Wang, *Int. J. Nanomed.* **2012**, *7*, 4185.
- [28] T. Y. Li, J. Benduhn, Z. Qiao, Y. Liu, Y. Li, R. Shivhare, F. Jaiser, P. Wang, J. Ma, O. Zeika, D. Neher, S. C. B. Mannsfeld, Z. Ma, K. Vandewal, K. Leo, *J. Phys. Chem. Lett.* **2019**, *10*, 2684.
- [29] a) K. Sun, Z. Xiao, S. Lu, W. Zajackowski, W. Pisula, E. Hanssen, J. M. White, R. M. Williamson, J. Subbiah, J. Ouyang, A. B. Holmes, W. W. Wong, D. J. Jones, *Nat. Commun.* **2015**, *6*, 6013; b) G. Li, X. Zhang, L. O. Jones, J. M. Alzola, S. Mukherjee, L. W. Feng, W. Zhu, C. L. Stern, W. Huang, J. Yu, V. K. Sangwan, D. M. DeLongchamp, K. L. Kohlstedt, M. R. Wasielewski, M. C. Hersam, G. C. Schatz, A. Facchetti, T. J. Marks, *J. Am. Chem. Soc.* **2021**, *143*, 6123.
- [30] a) N. N. Bie, T. Y. Yong, Z. H. Wei, Q. L. Liang, X. Q. Zhang, S. Y. Li, X. Li, J. Y. Li, L. Gan, X. L. Yang, *Signal Transduct. Tar.* **2023**, *8*, 408; b) Y. Zeng, S. Li, S. Zhang, L. Wang, H. Yuan, F. Hu, *Acta Pharm. Sin. B* **2022**, *12*, 3233.
- [31] a) Y. Dong, S. Dong, C. Yu, J. Liu, S. Gai, Y. Xie, Z. Zhao, X. Qin, L. Feng, P. Yang, Y. Zhao, *Sci. Adv.* **2023**, *9*, ead19980; b) J. Zhuang, Z. Ma, N. Li, H. Chen, L. Yang, Y. Lu, K. Guo, N. Zhao, B. Z. Tang, *Adv. Mater.* **2024**, *36*, 2309488.
- [32] a) X. Yuan, Y. Kang, J. Dong, R. Li, J. Ye, Y. Fan, J. Han, J. Yu, G. Ni, X. Ji, D. Ming, *Nat. Commun.* **2023**, *14*, 5140; b) Y. Fan, J. Ye, Y. Kang, G. Niu, J. Shi, X. Yuan, R. Li, J. Han, X. Ji, *Sci. Adv.* **2024**, *10*, eadm9561.
- [33] Y. Zhang, J. Chen, L. Shi, F. Ma, *Mater. Horiz.* **2023**, *10*, 361.
- [34] a) D. Wang, Z. Yu, Y. Qi, K. Hu, T. Zhou, J. Liu, W. Rao, *ACS Nano* **2023**, *17*, 13278; b) L. Yu, M. Yu, W. Chen, S. J. Sun, W. X. Huang, T. Q. Wang, Z. W. Peng, Z. W. Luo, Y. X. Wang, Y. J. Li, Y. Deng, M. Y. Wu, W. Tao, *J. Am. Chem. Soc.* **2023**, *145*, 8375.
- [35] a) Y. Agarwal, L. E. Milling, J. Y. H. Chang, L. Santollani, A. Sheen, E. A. Lutz, A. Tabet, J. Stinson, K. Ni, K. A. Rodrigues, T. J. Moyer, M. B. Melo, D. J. Irvine, K. D. Wittrup, *Nat. Biomed. Eng.* **2022**, *6*, 129; b) D. Laera, H. HogenEsch, D. T. O'Hagan, *Pharmaceutics* **2023**, *15*.
- [36] a) X. Zhong, C. Li, G. Zhao, M. Li, S. Chen, Y. Cao, Q. Wang, J. Sun, S. Zhu, S. Chang, *J. Nanobiotechnol.* **2022**, *20*, 468; b) E. A. Lutz, Y. Agarwal, N. Momin, S. C. Cowles, J. R. Palmeri, E. Duong, V. Hornet, A. Sheen, B. M. Lax, A. M. Rothschilds, D. J. Irvine, S. Spranger, K. D. Wittrup, *Proc. Natl. Acad. Sci. U.S.A.* **2022**, *119*, e2205983119.
- [37] A. Del Prete, V. Salvi, A. Soriani, M. Laffranchi, F. Sozio, D. Bosisio, S. Sozzani, *Cell Mol. Immunol.* **2023**, *20*, 432.
- [38] a) G. Kroemer, C. Galassi, L. Zitvogel, L. Galluzzi, *Nat. Immunol.* **2022**, *23*, 487; b) Z. Zeng, C. Zhang, S. He, J. Li, K. Pu, *Adv. Mater.* **2022**, *34*, 2203246.
- [39] Z. Xiao, T. Li, X. Zheng, L. Lin, X. Wang, B. Li, J. Huang, Y. Wang, X. Shuai, K. Zhu, *Bioact. Mater.* **2023**, *21*, 57.
- [40] M. Ding, Y. Zhang, N. Yu, J. Zhou, L. Zhu, X. Wang, J. Li, *Adv. Mater.* **2023**, *35*, 2302508;